



# PHANGS–JWST First Results: Variations in PAH Fraction as a Function of ISM Phase and Metallicity

Jérémy Chastenet<sup>1</sup> , Jessica Sutter<sup>2</sup> , Karin Sandstrom<sup>2</sup> , Francesco Belfiore<sup>3</sup> , Oleg V. Egorov<sup>4</sup> , Kirsten L. Larson<sup>5</sup> , Adam K. Leroy<sup>6</sup> , Daizhong Liu<sup>7</sup> , Erik Rosolowsky<sup>8</sup> , David A. Thilker<sup>9</sup> , Elizabeth J. Watkins<sup>4</sup> , Thomas G. Williams<sup>10,11</sup> , Ashley. T. Barnes<sup>12</sup> , Frank Bigiel<sup>12</sup> , Médéric Boquien<sup>13</sup> , Mélanie Chevance<sup>14,15</sup> , I-Da Chiang (江宜達)<sup>16</sup> , Daniel A. Dale<sup>17</sup> , J. M. Diederik Kruijssen<sup>15</sup> , Eric Emsellem<sup>18,19</sup> , Kathryn Grasha<sup>20,21</sup> , Brent Groves<sup>22</sup> , Hamid Hassani<sup>8</sup> , Annie Hughes<sup>23</sup> , Kathryn Kreckel<sup>4</sup> , Sharon E. Meidt<sup>1</sup> , Ryan J. Rickards Vaught<sup>2</sup> , Amy Sardone<sup>24,25</sup> , and Eva Schinnerer<sup>11</sup>

<sup>1</sup> Sterrenkundig Observatorium, Ghent University, Krijgslaan 281-S9, B-9000 Gent, Belgium; [jeremy.chastenet@ugent.be](mailto:jeremy.chastenet@ugent.be)

<sup>2</sup> Center for Astrophysics and Space Sciences, Department of Physics, University of California, San Diego 9500 Gilman Drive, La Jolla, CA 92093, USA

<sup>3</sup> INAF—Arcetri Astrophysical Observatory, Largo E. Fermi 5, I-50125, Florence, Italy

<sup>4</sup> Astronomisches Rechen-Institut, Zentrum für Astronomie der Universität Heidelberg, Mönchhofstraße 12-14, D-69120 Heidelberg, Germany

<sup>5</sup> AURA for the European Space Agency (ESA), Space Telescope Science Institute, 3700 San Martin Drive, Baltimore, MD 21218, USA

<sup>6</sup> Department of Astronomy, The Ohio State University, 140 West 18th Avenue, Columbus, Ohio 43210, USA

<sup>7</sup> Max-Planck-Institut für Extraterrestrische Physik (MPE), Giessenbachstr. 1, D-85748 Garching, Germany

<sup>8</sup> Department of Physics, University of Alberta, Edmonton, Alberta, T6G 2E1, Canada

<sup>9</sup> Department of Physics and Astronomy, The Johns Hopkins University, Baltimore, MD 21218, USA

<sup>10</sup> Sub-department of Astrophysics, Department of Physics, University of Oxford, Keble Road, Oxford OX1 3RH, UK

<sup>11</sup> Max-Planck-Institut für Astronomie, Königstuhl 17, D-69117, Heidelberg, Germany

<sup>12</sup> Argelander-Institut für Astronomie, Universität Bonn, Auf dem Hügel 71, D-53121, Bonn, Germany

<sup>13</sup> Centro de Astronomia (CITEVA), Universidad de Antofagasta, Avenida Angamos 601, Antofagasta, Chile

<sup>14</sup> Institut für Theoretische Astrophysik, Zentrum für Astronomie der Universität Heidelberg, Albert-Ueberle-Strasse 2, D-69120 Heidelberg, Germany

<sup>15</sup> Cosmic Origins Of Life (COOL) Research DAO

<sup>16</sup> Institute of Astronomy and Astrophysics, Academia Sinica, No. 1, Sec. 4, Roosevelt Road, Taipei 10617, Taiwan

<sup>17</sup> Department of Physics and Astronomy, University of Wyoming, Laramie, WY 82071, USA

<sup>18</sup> European Southern Observatory, Karl-Schwarzschild-Straße 2, D-85748 Garching, Germany

<sup>19</sup> Univ Lyon, Univ Lyon1, ENS de Lyon, CNRS, Centre de Recherche Astrophysique de Lyon UMR5574, F-69230 Saint-Genis-Laval France

<sup>20</sup> Research School of Astronomy and Astrophysics, Australian National University, Canberra, ACT 2611, Australia

<sup>21</sup> Research School of Astronomy and Astrophysics, Australian National University, Canberra, ACT 2611; Centre of Excellence for All Sky Astrophysics in 3 Dimensions (ASTRO 3D), Australia

<sup>22</sup> International Centre for Radio Astronomy Research, University of Western Australia, 7 Fairway, Crawley, 6009 WA, Australia

<sup>23</sup> IRAP, Université de Toulouse, CNRS, CNES, UPS, (Toulouse), France

<sup>24</sup> Department of Astronomy, The Ohio State University, 140 West 18th Avenue, Columbus, OH 43210, USA

<sup>25</sup> Center for Cosmology and Astroparticle Physics, 191 West Woodruff Avenue, Columbus, OH 43210, USA

Received 2022 October 21; revised 2022 November 30; accepted 2022 December 22; published 2023 February 16

## Abstract

We present maps tracing the fraction of dust in the form of polycyclic aromatic hydrocarbons (PAHs) in IC 5332, NGC 628, NGC 1365, and NGC 7496 from JWST/MIRI observations. We trace the PAH fraction by combining the F770W (7.7  $\mu\text{m}$ ) and F1130W (11.3  $\mu\text{m}$ ) filters to track ionized and neutral PAH emission, respectively, and comparing the PAH emission to F2100W, which traces small, hot dust grains. We find the average  $R_{\text{PAH}} = (\text{F770W} + \text{F1130W})/\text{F2100W}$  values of 3.3, 4.7, 5.1, and 3.6 in IC 5332, NGC 628, NGC 1365, and NGC 7496, respectively. We find that H II regions traced by MUSE H $\alpha$  show a systematically low PAH fraction. The PAH fraction remains relatively constant across other galactic environments, with slight variations. We use CO+HI +H $\alpha$  to trace the interstellar gas phase and find that the PAH fraction decreases above a value of  $I_{\text{H}\alpha}/\Sigma_{\text{HI}+\text{H}_2} \sim 10^{37.5} \text{ erg s}^{-1} \text{ kpc}^{-2} (M_{\odot} \text{ pc}^{-2})^{-1}$  in all four galaxies. Radial profiles also show a decreasing PAH fraction with increasing radius, correlated with lower metallicity, in line with previous results showing a strong metallicity dependence to the PAH fraction. Our results suggest that the process of PAH destruction in ionized gas operates similarly across the four targets.

*Unified Astronomy Thesaurus concepts:* [Dust physics \(2229\)](#); [Interstellar dust \(836\)](#); [Polycyclic aromatic hydrocarbons \(1280\)](#)

## 1. Introduction

The mid-infrared (mid-IR) emission features at 3.3, 6.2, 7.7, 8.6, 11.3, 12.6, and 17  $\mu\text{m}$  are characteristic of the aromatic content of interstellar dust (see reviews from Draine 2003;

Tielens 2008; Li 2020). The carriers of these features are often referred to as polycyclic aromatic hydrocarbons (PAHs; Allamandola et al. 1985) and have been included as an extension of carbonaceous grains to small sizes in several physical dust models (e.g., Desert et al. 1990; Zubko et al. 2004; Draine & Li 2007; Galliano et al. 2008) or as an aromatic-rich mantle covering aliphatic grains (e.g., Jones et al. 2017 and reference therein). For the rest of this Letter, we will refer to the carriers of mid-IR features as PAHs.

Original content from this work may be used under the terms of the [Creative Commons Attribution 4.0 licence](#). Any further distribution of this work must maintain attribution to the author(s) and the title of the work, journal citation and DOI.

**Table 1**

R.A. (R. A.) and decl. (Decl.) Coordinates (J2000), the  $r_{25}$  Radius, in Arcminutes, Used in This Letter for Our Four Targets, from the HyperLeda Database (Makarov et al. 2014)

Target	R. A.	Decl.	Distance (Mpc)	P.A. (°)	$i$ (°)	$r_{25}$ (′)	$\langle R_{\text{PAH}} \rangle$	16th–84th percentiles
IC 5332	23:34:27.488	−36:06:3.89	9.01	74.4	26.9	3.03	3.3	1.8–4.8
NGC 628	01:36:41.745	+15:47:1.11	9.84	20.7	8.9	4.94	4.7	3.8–5.6
NGC 1365	03:33:36.458	−36:08:26.37	19.57	201.1	55.4	6.01	5.1	3.8–6.3
NGC 7496	23:09:47.288	−43:25:40.28	18.72	193.7	35.9	1.67	3.6	1.8–5.3

**Note.** Distances are from Anand et al. (2021). Position angles and inclinations are from Leroy et al. (2021b). Additional information can be found in Table 1 of the survey paper (Lee et al. 2023). The second part of the table shows the mean and 16th–84th percentiles of  $R_{\text{PAH}}$ .

The (collective) brightness of these features with respect to a dust continuum emission can be used as a tracer of the fraction of dust in the form of PAHs. The mass fraction of PAHs can be measured from fitting models to observed dust emission measured from mid- through far-IR broadband photometry (e.g., Draine et al. 2007; Galliano et al. 2008; Galliano 2018; Chastenet et al. 2019; Nersesian et al. 2019; Aniano et al. 2020). One can also fit mid-IR spectra and derive more detailed information about the relative intensities of each feature, like the average charge and size of the PAH population (Smith et al. 2007; Lai et al. 2020; Maragkoudakis et al. 2022). As very prominent features, the emission at 7.7 and 11.3  $\mu\text{m}$  can be considered a satisfactory proxy to trace the total emission from PAHs in normal star-forming galaxies (e.g., Smith et al. 2007; Lai et al. 2020; Draine et al. 2021).

PAHs also play a key role in heating the interstellar medium (ISM) within photodissociation regions (PDRs; Bakes & Tielens 1994; Weingartner & Draine 2001; Tielens 2008; Berné et al. 2009; Croxall et al. 2012; Wolfire et al. 2022). As a significant source of photoejected electrons, the abundance of PAHs greatly influences the photoelectric heating efficiency. The close tie between PAHs and PDR heating has led to the suggested use of PAH emission as a tracer of the star formation rate (e.g., Peeters et al. 2004; Shipley et al. 2016).

The variations of the PAH fraction in the ISM of external galaxies help us to understand their origin and evolution, as well as the mechanisms that regulate their formation and destruction. Several studies have found that the fraction of PAHs decreases in regions of ionized gas and/or because of hard radiation fields (e.g., Giard et al. 1994; Dong & Draine 2011; Verstraete 2011; Salgado et al. 2016; Chastenet et al. 2019; Rigopoulou et al. 2021), as theory predicts (Siebenmorgen et al. 2004; Groves et al. 2008; Micelotta et al. 2010; Bocchio et al. 2012; Zhen et al. 2016), and becomes very low in H II regions (e.g., Pety et al. 2005; Lebouteiller et al. 2007; Thilker et al. 2007; Compiègne et al. 2008). There is also evidence of a correlation of PAH features with the CO content (see, e.g., Leroy et al. 2023). Studying nearby galaxies, Regan et al. (2006) found that the 8  $\mu\text{m}$  (traced by Spitzer/IRAC) and CO radial profiles are closely matched. Evidence of a close link between PAH and CO emission has also been observed in high-redshift galaxies on galactic scales (e.g., Pope et al. 2013; Cortzen et al. 2019).

In addition to trends observed across different ISM environments, the abundance of PAHs has been shown to decrease in low-metallicity galaxies (e.g., Draine et al. 2007; Engelbracht et al. 2008; Sandstrom et al. 2012). This deficit in PAHs has multiple proposed causes, including the destruction of PAHs by hard radiation fields present in low-metallicity

galaxies (Madden et al. 2006; Gordon et al. 2008) or delayed PAH formation in asymptotic giant branch star atmospheres (Galliano et al. 2008). These trends have important implications for future observations of PAH emission in high-redshift galaxies, making it essential to study PAH variation across a range of systems. By further establishing how metallicity trends can lead to the reduction in PAH emission, we will be better prepared for using these small grains to assess ISM conditions across cosmic time.

The recent launch of JWST opens a new window for exploring this question. The MIRI F770W and F1130W filters provide coverage of two of the most prominent PAH features at 7.7 and 11.3  $\mu\text{m}$ , while the F2100W filter lends a useful comparison, tracing emission from larger dust grains (Draine & Li 2007). The unique ability of the MIRI instrument to map these PAH features at unprecedented resolution and sensitivity in galaxies outside of the Local Group allows us to greatly expand the range of ISM conditions in which measurements of the PAH fraction can be made and better determine how the local ISM conditions can influence the relative amount of PAHs present.

In this Letter, we investigate the variations of the PAH fraction traced by a combination of JWST/MIRI filters across the full disk of four nearby galaxies, IC 5332, NGC 628, NGC 1365, and NGC 7496. By tracking the PAH fraction across the multiphase ISM, we are able to determine how a range of ISM properties affect the relative abundance of PAHs with respect to large dust grains. This will lay the groundwork for more detailed studies of how PAH emission varies in specific conditions, such as those found around sites of active star formation.

## 2. Data

### 2.1. JWST/MIRI Data

The data used in this paper are part of the PHANGS–JWST Treasury program #2107 (PI: J.C. Lee; Lee et al. 2023). We use MIRI (Rieke et al. 2015) observations in the F770W, F1130W, and F2100W filters, from the latest reference files at the time of processing, as described by Lee et al. (2023) and Leroy et al. (2023). The PHANGS–JWST team used the STScI Calibration pipeline 1.7.1 for NIRCcam and 1.7.0 for MIRI and Calibration Reference Data context number 0968 for both instruments. Table 1 gives a few key details about the four targets of this Letter, which are used to construct  $r/r_{25}$  maps.

We convolve all three filter maps to 1'' resolution, which is larger than the full width at half maximum of the F2100W filter (0.''67). The convolution kernels were computed using the theoretical point-spread functions (PSFs) of each filter provided

by the WEBBPSF (Perrin et al. 2014) and the method described in Aniano et al. (2011). We choose to slightly degrade the data to increase the signal-to-noise ratio (S/N) in the F2100W band. By doing so, we are also able to match the resolution of the CO and H $\alpha$  data (see Section 2.2).

## 2.2. Ancillary Data

We use  $^{12}\text{CO}(2-1)$  “broad” moment 0 maps and corresponding error maps from the PHANGS–ALMA survey combining 12m + 7m + Total Power (Leroy et al. 2021a, 2021b) to trace molecular gas at  $\sim 1''$  ( $\sim 40$ – $90$  pc in our sample) resolution. To convert CO intensity to molecular gas surface density,  $\Sigma_{\text{H}_2}$  in  $M_{\odot} \text{pc}^{-2}$ , we use a constant CO-to-H $_2$  conversion factor  $\alpha_{\text{CO}} = 4.35 M_{\odot} \text{pc}^{-2} (\text{K km s}^{-1})^{-1}$  as recommended for solar metallicity, star-forming galaxies (Bolatto et al. 2013),<sup>26</sup> and a  $^{12}\text{CO}(2-1)/^{12}\text{CO}(1-0)$  line ratio  $R_{21} = 0.65$  (den Brok et al. 2021; Leroy et al. 2022).

We use H $\alpha$  maps from the PHANGS–MUSE survey (Emsellem et al. 2022) to trace ionized gas. We use the “native” resolution maps with an average  $\sim 0''.8$  resolution and a  $0''.2$  pixel size. To trace the  $12 + \log(\text{O}/\text{H})$  metallicity in our targets, we use the 2D maps by Williams et al. (2022). The maps were created by interpolating H II regions-derived metallicity maps (with S-calibration), using a Gaussian process regression technique, based on PHANGS–MUSE maps of H $\alpha$  intensity. These maps have fixed physical- and different angular resolutions (Emsellem et al. 2022), all lower than  $1''$  except for NGC 1365 ( $1''.15$ ). We convolve all maps with a resolution lower than  $1''$  to that value, to match the convolved MIRI maps.

We use HI measurements from MeerKAT (C. Eibensteiner et al. 2022, in preparation), at  $15''$  resolution for NGC 7496 and from THINGS (Walter et al. 2008) for NGC 628 ( $\sim 11''$  for the “natural” weighted map). We convert the maps to have units of atomic gas mass surface density including helium, assuming optically thin 21 cm emission, using the prescription from Leroy et al. (2012; see also Walter et al. 2008, 2008). We lack resolved 21 cm mapping for IC 5332 and NGC 1365. Based on the observed flatness of the atomic gas surface density over the inner parts of galaxy disks (e.g., Schrubba et al. 2011; Bigiel & Blitz 2012; Kennicutt & Evans 2012; Wong et al. 2013), we assume that the atomic gas has a flat distribution with  $\Sigma_{\text{HI}} = 8 M_{\odot} \text{pc}^{-2}$  (including helium). The HI data have the lowest resolution among the data sets for our sample. Since the HI distribution is expected to be reasonably smooth across the disk of all our targets (as a likely result of low resolution; Leroy et al. 2013), we choose to work at the MIRI F2100W resolution to retain as much information about the distribution of the PAH emission within galaxies as possible. We reproject these maps to the MIRI pixel grid with pixel size  $\sim 0''.11$ .

## 2.3. Noise Properties and Masks

We measure background standard deviation in NGC 7496 as it is the only one that offers enough pixels off target, at  $1''$  resolution. Lee et al. (2023) give details of the reduction of the data, including noise. The background removal is done by anchoring the JWST data with Spitzer, where the background in these sources was better estimated. This is done as few off-source pixels are available in most of the early targets. We find

that MIRI maps have similar noise, and we assume NGC 7496 estimates throughout the sample. We remove pixels with  $S/N \leq 3$  in all MIRI bands, with background noise values of 0.05, 0.05, and  $0.1 \text{ MJy sr}^{-1}$ . In NGC 1365 and NGC 7496, we mask pixels in the center due to IR brightness of the active galactic nuclei (AGNs), which saturate the signal mostly in the F2100W band. This is done using the WEBBPSF package (Perrin et al. 2014) and centering the F2100W PSF on the central coordinates of each target. For this preliminary work, we remove additional conspicuous artifacts from the central AGN that remain after this analysis. These spikes are due to the central saturation, and although they are not flagged as “bad pixels” by data reduction, they are an obvious artifact. We mask these by hand to ensure they do not bias our initial results. They are shown in gray scale in Figure 1 but are not used in the analysis.

## 3. PAH Fraction

In Draine et al. (2021), the authors found that the luminosity of the  $7.7 \mu\text{m}$  feature<sup>27</sup> normalized to the total IR luminosity can approximate the PAH fraction in all but the most extreme cases (Draine & Li 2007; Draine et al. 2021). Here, we use the JWST/MIRI  $R_{\text{PAH}} = (F770W + F1130W)/F2100W$  ratio as a proxy for the PAH fraction. Over a broad range of PAH size (in terms of number of carbon atoms) and assuming a Galactic interstellar radiation field (Mathis et al. 1983; at 10 kpc), the  $7.7 \mu\text{m}$  feature is more representative of the ionized PAH population and the  $11.3 \mu\text{m}$  feature of the neutral population (e.g., Rapacioli et al. 2005; Draine et al. 2021). We assume the F2100W filter is free from contribution from PAHs and is instead dominated by small, hot dust grains, as seen in the Spitzer/Infrared Spectrograph spectra of local galaxies observed by the SINGS project (Smith et al. 2007; see also Draine & Li 2007, 2007; Dale et al. 2009, 2009). This assumption is validated by a clear difference in behavior between the F2100W and PAH-dominated band emission, demonstrated in Leroy et al. (2023). Normalizing the emission at  $7.7$  and  $11.3 \mu\text{m}$  by the observed flux at  $21 \mu\text{m}$  help us focus on the PAH-only fraction. Previous studies of the PAH population in nearby galaxies completed with Spitzer have shown that the ratio of  $8$ – $24 \mu\text{m}$  is a good tracer of the PAH fraction (see e.g., Smith et al. 2007; Marble et al. 2010; Croxall et al. 2012). In addition, models of PAH and dust emission have shown  $7.7 \mu\text{m}$ -to-total IR luminosity is a good tracer the PAH mass fraction ( $q_{\text{PAH}}$ ; Draine & Li 2007). Using the MIRI filters, we can improve on this by using the bands centered on the PAH features (F770W and F1130W) in place of the  $8 \mu\text{m}$  data while the F2100W replaces the  $24 \mu\text{m}$  continuum tracer. As both the PAH features and the  $21 \mu\text{m}$  continuum are from stochastic heating, using these fluxes to determine the PAH fraction removes any significant dependence on the radiation field (except in extreme situations; see Draine & Li 2007, their Figure 13).

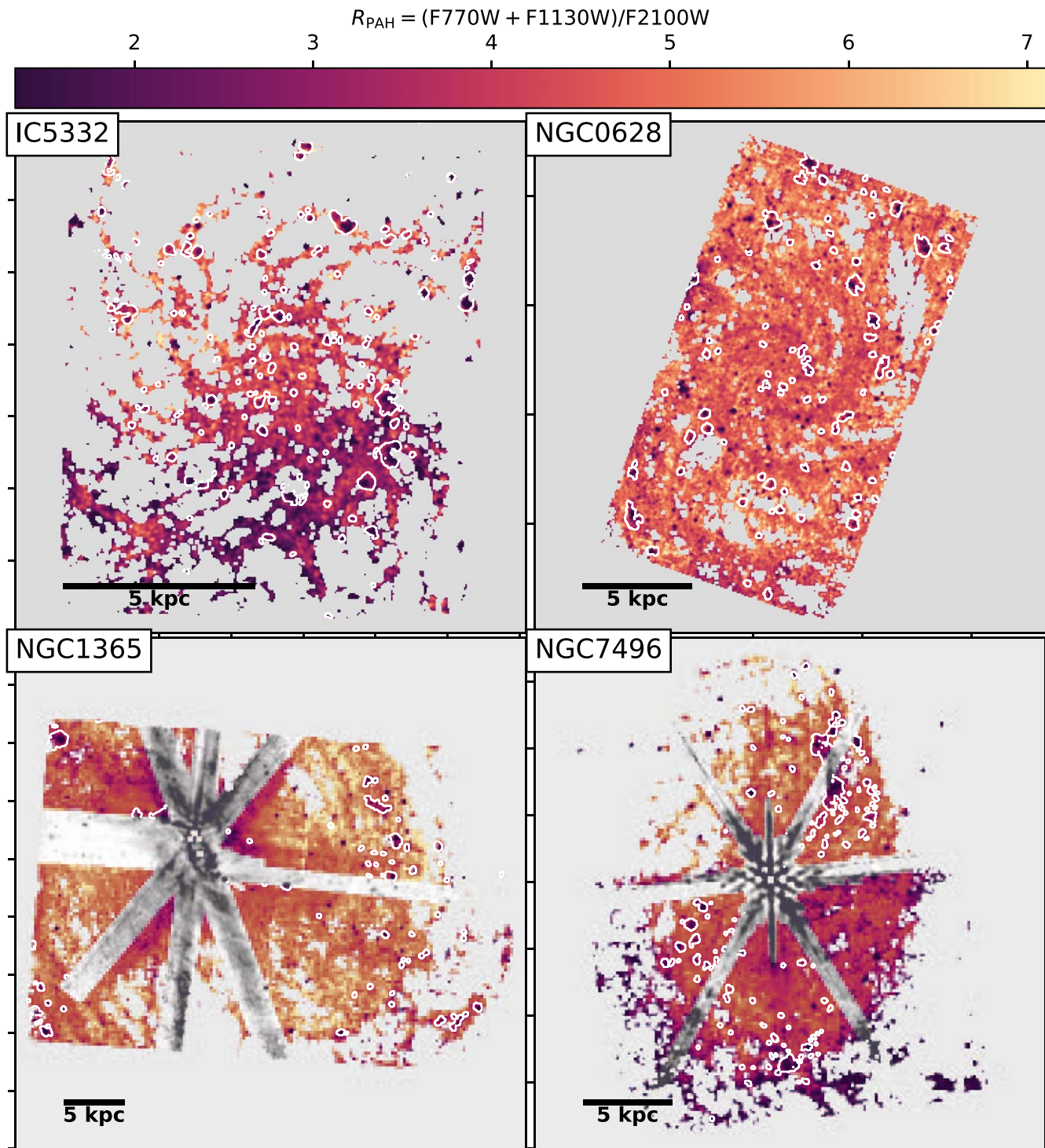
### 3.1. Qualitative Description

Figure 1 shows  $R_{\text{PAH}}$  in the four PHANGS–JWST early targets. The white contours show the brightest H II regions

<sup>26</sup> With the assumption of a flat HI distribution, the choice of  $\alpha_{\text{CO}}$  is not the dominant uncertainty.

<sup>27</sup> In this model, the  $7.7 \mu\text{m}$  feature luminosity is determined by integrating between two set “clip” points,  $\lambda = 6.9$  and  $\lambda = 9.7$ . This is not exactly equal to fluxes observed using the F770W filter, which spans  $\lambda = 6.6$ – $8.6$ , but is similar.





**Figure 1.** Maps of  $R_{\text{PAH}}$  in IC 5332 (top left), NGC 628 (top right), NGC 1365 (bottom left), and NGC 7496 (bottom right). We mask the pixels with an  $S/N < 3$  in all bands (gray uniform background). We also mask the central pixels in NGC 1365 and NGC 7496 that are saturated, using instrument PSFs, and perform a by-hand additional masking to remove conspicuous saturation artifacts (shown in gray scale, not included in the analysis). We plot contours for a few of the brightest H II regions. They are clearly visible as depressions (darker colors) in  $R_{\text{PAH}}$ , especially in NGC 628 and NGC 7496.

(Groves et al. 2023; Santoro et al. 2022). In all cases, it appears that  $R_{\text{PAH}}$  shows clear depressions within H II regions though NGC 628 and NGC 7496 show this contrast most clearly.

In the right section of Table 1, we show the mean of the ratio,  $\langle R_{\text{PAH}} \rangle$ , and the associated 16th–84th percentile range. NGC 1365 shows the highest average for  $R_{\text{PAH}}$  and IC 5332 the lowest. All 16th–84th ranges agree reasonably well, and

NGC 7496 shows the broadest range. The top left panel of Figure 2 shows the radial profiles of  $R_{\text{PAH}}$  in bins of  $r/r_{25}$ . In all panels, the error bars are 3 times the standard error of the mean (SEM). These errors are small because of the number of pixels in each bin (the standard deviation is much larger). Note that not all galaxies have observations extending to the same  $r/r_{25}$ .

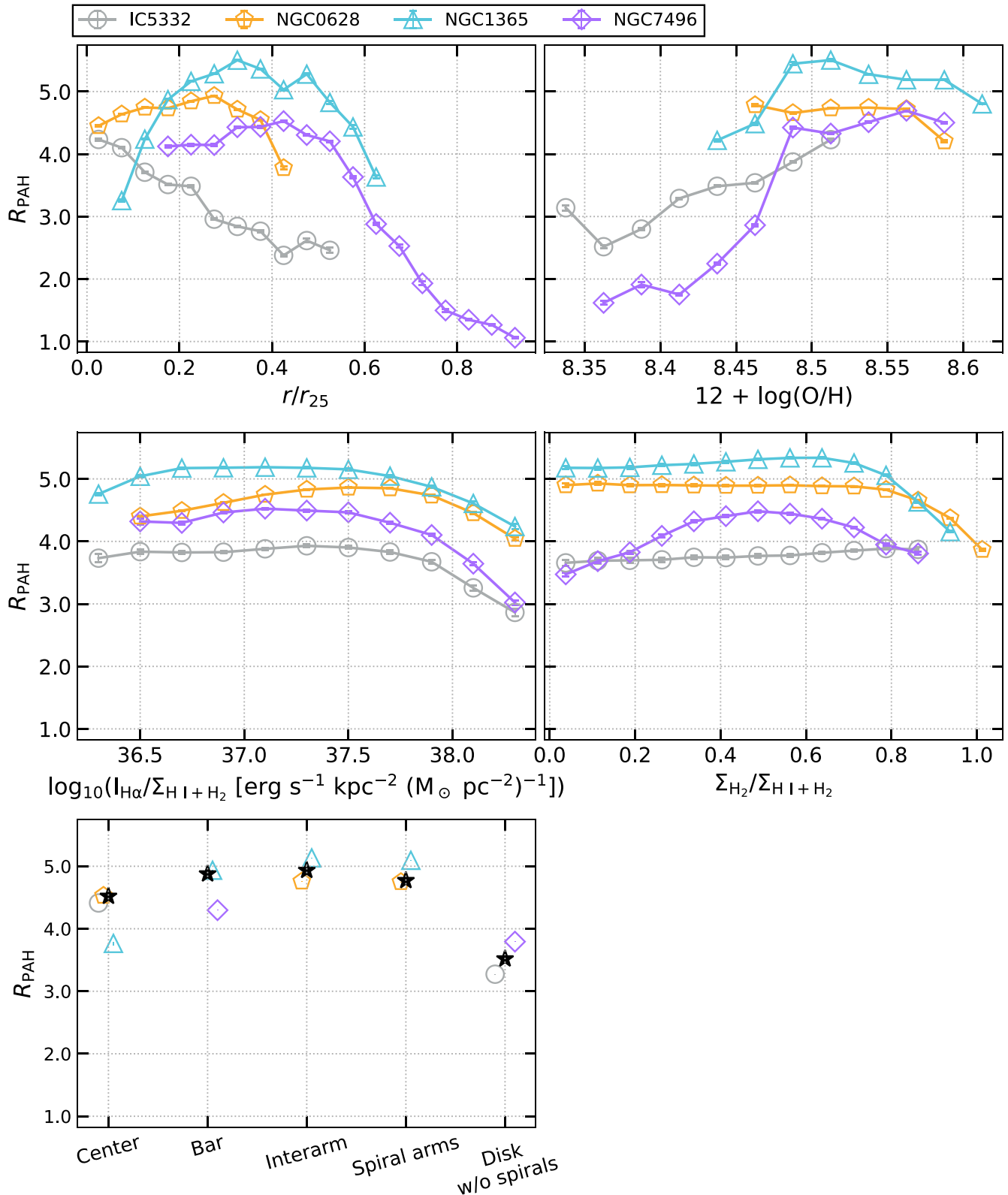


**Figure 2.** Running medians of  $R_{\text{PAH}}$  as a function of the following: (top left)  $r/r_{25}$ ; (top right)  $12 + \log(\text{O}/\text{H})$ , using metallicity maps from Williams et al. (2022); (middle left)  $I_{\text{H}\alpha}/\Sigma_{\text{HI}+\text{H}_2}$  in units of  $\text{erg s}^{-1} \text{kpc}^{-2} (M_{\odot} \text{pc}^{-2})^{-1}$ ; (middle right) the fraction of molecular gas; and (bottom left) the environmental masks from Querejeta et al. (2021), with a filled black star showing the median for all pixels within each category. The error bars show  $3 \times \text{SEM}$  in each bin (except for the bottom left panel; only  $1 \text{ SEM}$ ). Note that the middle panels involve the flat HI distribution assumption in IC 5332 and NGC 1365, which may shift the curves horizontally.

All galaxies show an overall decreasing trend with radius. There is, however, a slightly different trend in NGC 1365 and NGC 7496, which both show an increase in abundance ratio at

small radii before exhibiting a steady decrease. Both are Seyfert galaxies (NGC 1365: 1.8, NGC 7496: 2.0; e.g., García-Bernete et al. 2022) hosting an AGN as well as central bars that feed

high-density regions at their centers. Even though we mask the region around the AGN, this increasing trend at small radii could be due to the influence of the central AGN on the PAH population. The definitive impact of AGNs on the PAH population is not yet completely clear. For example, García-Bernete et al. (2022) found differences in the relative strengths of different PAH features in AGN host galaxies and star-forming galaxies at kiloparsec scales. However, Lai et al. (2022) recently found relatively small variations in PAH size and ionization and a decrease in PAH emission only in the *direct* line of sight of the AGN, using JWST observations. Similarly, Viaene et al. (2020) found that the influence of the AGN is only relevant close to the nucleus. Additionally, there is evidence for PAH molecules surviving the harsh environment surrounding AGNs (e.g., Alonso-Herrero et al. 2014; Jensen et al. 2017; García-Bernete et al. 2022). Although we observe a decreasing trend in these two galaxies toward the center, it is as of yet uncertain how the presence of an AGN may be related to this decrease. Additional work will be required to clearly understand the scales at which AGNs impact the global fraction of PAHs.

We also show the profile of  $R_{\text{PAH}}$  with  $12 + \log(\text{O}/\text{H})$  metallicity in the top right panel of Figure 2. Global trends of the PAH fraction with metallicity have been studied on integrated scales in several works (Draine et al. 2007; Rémy-Ruyer et al. 2015; Chastenet et al. 2019; Galliano et al. 2021). Here, we see that this trend is similar on small resolved scales ( $\sim$  tens of parsecs). The turning point in the metallicity value, where the abundance ratio starts to decrease with increasing metallicity, is similar to the downturn at small  $r/r_{25}$  as these are primarily radial metallicity gradients.

### 3.2. Variation of PAH Fraction with ISM Environment

In Figure 2, middle and bottom rows, we present the variation of  $R_{\text{PAH}}$  as a function of the ISM environment. We combine the HI and H<sub>2</sub> maps to estimate the total gas surface density and use the ratio of H $\alpha$  intensity to total gas to follow the variations of the ISM conditions in each target (in units of  $\text{erg s}^{-1} \text{kpc}^{-2} (M_{\odot} \text{pc}^{-2})^{-1}$ ). As we expect PAH emission to arise from a range of ISM phases, the ratio of H $\alpha$  intensity to total gas ( $I_{\text{H}\alpha}/\Sigma_{\text{HI}+\text{H}_2}$ ) is used as a proxy for environments dominated by the ionized phase and can provide a clear indication of what ISM environments the PAH emission is coming from. For example, high values of  $I_{\text{H}\alpha}/\Sigma_{\text{HI}+\text{H}_2}$  are indicative of regions dominated by ionized gas, while low values of  $I_{\text{H}\alpha}/\Sigma_{\text{HI}+\text{H}_2}$  suggest the dominance of neutral gas. This comparison works well because neutral and ionized gas are decorrelated on small spatial scales and the clearing of neutral gas due to rapid ionizing feedback ( $<5$  Myr; Kruijssen et al. 2019; Chevance et al. 2020, 2022; Kim et al. 2022). By comparing  $R_{\text{PAH}}$  to  $I_{\text{H}\alpha}/\Sigma_{\text{HI}+\text{H}_2}$  we can better understand what ISM conditions, i.e., what fraction of the line of sight is ionized gas free of PAHs, could lead to an observed dearth of PAH emission. This is further investigated within HII regions in Egorov et al. (2023).

The middle left panel of Figure 2 shows the variations of  $R_{\text{PAH}}$  as a function of  $I_{\text{H}\alpha}/\Sigma_{\text{HI}+\text{H}_2}$ . The abundance of PAHs appears to stay rather flat until a threshold in  $I_{\text{H}\alpha}/\Sigma_{\text{HI}+\text{H}_2}$ , where it decreases steeply. This is expected from the destruction of PAHs in harsh environments traced by high-intensity H $\alpha$  (e.g., Groves et al. 2008; Micelotta et al. 2010; Bocchio et al. 2012; Egorov et al. 2023) and has been observed

in Galactic PDRs (Pety et al. 2005; Compiègne et al. 2008). Interestingly, it appears that all galaxies share similar thresholds in  $I_{\text{H}\alpha}/\Sigma_{\text{HI}+\text{H}_2}$ , at which the PAH fraction starts to decrease. These inflection points seem to be around  $\sim 37.5 \text{ erg s}^{-1} \text{kpc}^{-2} (M_{\odot} \text{pc}^{-2})^{-1}$  for all targets. However, it should be pointed out that there are (currently) no similar resolution HI data for IC 5332 and NGC 1365, and therefore a universal threshold across all environments is left for future studies. Considering  $I_{\text{H}\alpha}/\Sigma_{\text{HI}+\text{H}_2}$  traces the fraction of ionized gas per unit of total gas, this common threshold could be a limit at which the amount of radiation producing the intense H $\alpha$  emission is able to destroy the PAHs through sputtering, overcoming shielding from molecular gas and reducing the observed PAH fraction.

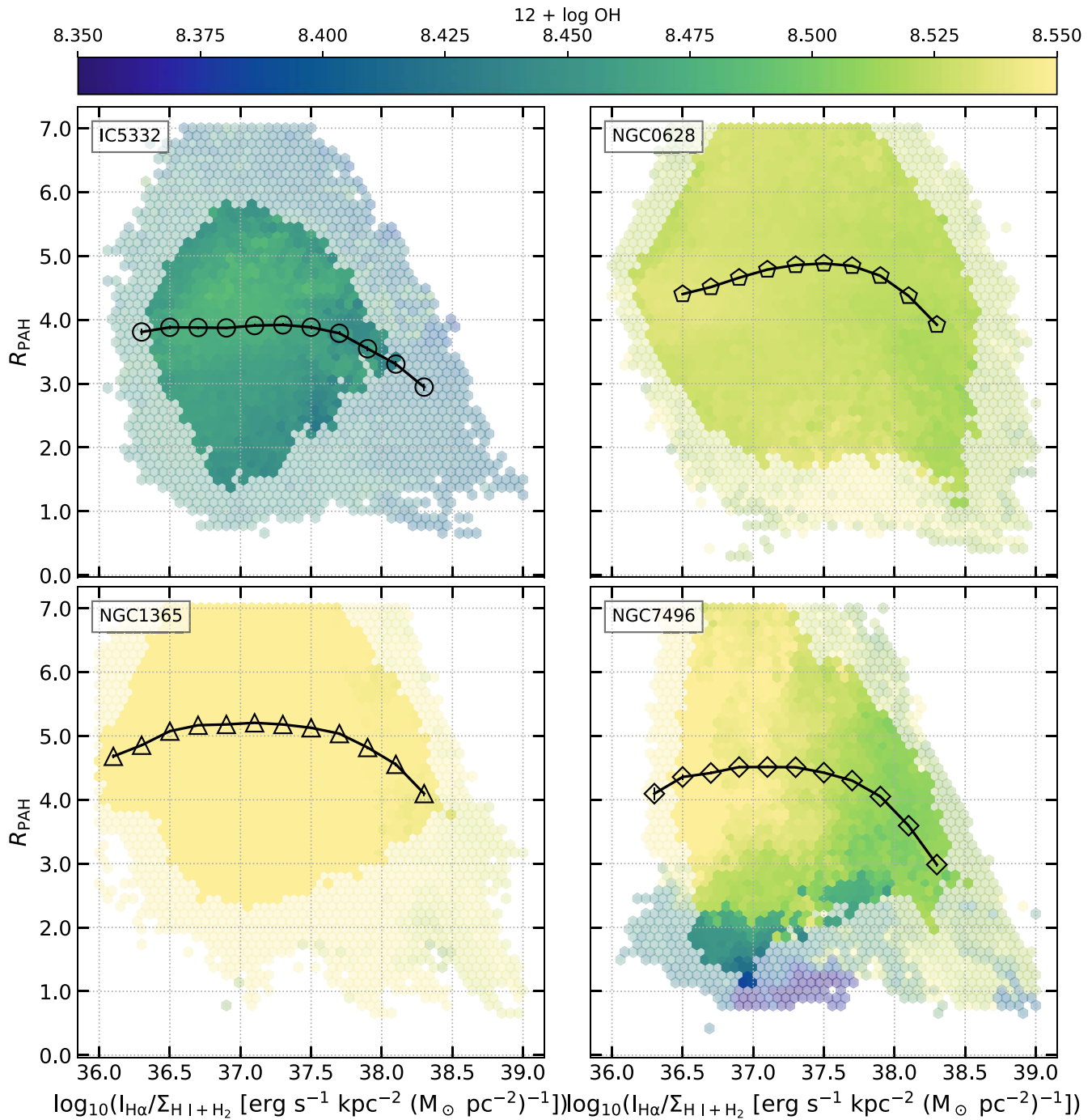
We can also see that there is an offset in PAH fraction, on average, between each galaxy (see also Table 1). Overall, this offset nicely tracks the global galaxy metallicity gradients (Kreckel et al. 2019; Groves et al. 2023; Santoro et al. 2022) in the lower H $\alpha$  intensity regions. As we move toward higher  $I_{\text{H}\alpha}/\Sigma_{\text{HI}+\text{H}_2}$  values, the offset gets minimized. This relates to results seen by Egorov et al. (2023), where no metallicity trend is found with  $R_{\text{PAH}}$  within HII regions. This suggests that the offset in PAH fraction between the four galaxies may be driven by a difference in the PAH population in the diffuse or neutral ISM set by the average metallicity of the galaxy. This general offset also follows trends observed in previous works that found that the PAH fraction correlates positively with metallicity in nearby galaxies (Draine et al. 2007; Rémy-Ruyer et al. 2015; Chastenet et al. 2019; Galliano et al. 2021) although it should be noted that the sample included in this work covers a small range of metallicity.

Figure 3 shows the same variations, with metallicity information. We show the 2D histograms of  $R_{\text{PAH}}$  as a function of  $I_{\text{H}\alpha}/\Sigma_{\text{HI}+\text{H}_2}$ , color coded by the median  $12 + \log(\text{O}/\text{H})$  metallicity in each bin. There is a visible color difference between each galaxy but no clear gradient. This implies that while the average metallicity of each galaxy seems to influence the PAH fraction, the moderate local metallicity variations are not having a large effect on  $R_{\text{PAH}}$ .

In the middle right panel of Figure 2, we show the variations of  $R_{\text{PAH}}$  as a function of the fraction of molecular gas to total cold gas fraction, as traced by CO. Behaviors vary between each galaxy, showing either a similar profile to that of  $R_{\text{PAH}}$  with  $I_{\text{H}\alpha}/\Sigma_{\text{HI}+\text{H}_2}$  (NGC 1365 and NGC 628 reflect the similarity in spatial distribution of CO and H $\alpha$  emission at these scales; Schinnerer et al. 2019), a rather flat trend (IC 5332, which has little CO), or a  $\sim 20\%$  increase to a maximum value, followed a decrease in  $R_{\text{PAH}}$  (NGC 7496). This could suggest that the abundance of PAHs is not particularly sensitive to the molecular fraction, compared to the ionized gas content. Chastenet et al. (2023) found that the average grain size of the global PAH population (as traced by the  $3.3/7.7 \mu\text{m}$  ratio; e.g., Maragkoudakis et al. 2020; Draine et al. 2021; Rigopoulou et al. 2021) is more sensitive to the fraction of molecular gas.

In the bottom left panel of Figure 2, we plot the median values of  $R_{\text{PAH}}$  in different galactic environments, identified by Querejeta et al. (2021). We use their spatial mask to separate pixels in five different categories (see their Table 1). Figure 4 shows the masks projected to the  $R_{\text{PAH}}$  maps, for a visual representation of the different environments. In the bottom-left panel of Figure 2, it appears that there is no





**Figure 3.** 2D histograms of the  $I_{H\alpha}/\Sigma_{HI+H_2}$  and the  $R_{PAH}$ , color coded by metallicity, using the gradient from PHANGS–MUSE. The more transparent colors indicate bins with at least 10 hits, while the solid colors indicate those with at least 100 hits per bin.

striking differences between environments, again showing minimal variations of a few tens of percent, for individual galaxies. We also show the median and associated SEM for *all* pixels falling into each category with black-filled star symbols. Here, we can see that  $R_{PAH}$  is the highest in the bar and interarm regions, with lower values in the spiral arms, followed by the center, and finally in the disk. Although this approach is limited by the number of targets at this stage, it shows promising results. The higher fraction of PAHs in the

interarms tracks with a less harsh environment due to star formation and a possibly more HI dominated ISM. Adding more targets to this approach will provide a generic view of the variation of the PAH fraction in the different phases of nearby galaxies.

Future work will improve on this work by more finely binning the data. For example, it will be interesting to investigate the sensitivity of each parameter to the S/N measured in the MIRI data. It will also be possible to test a

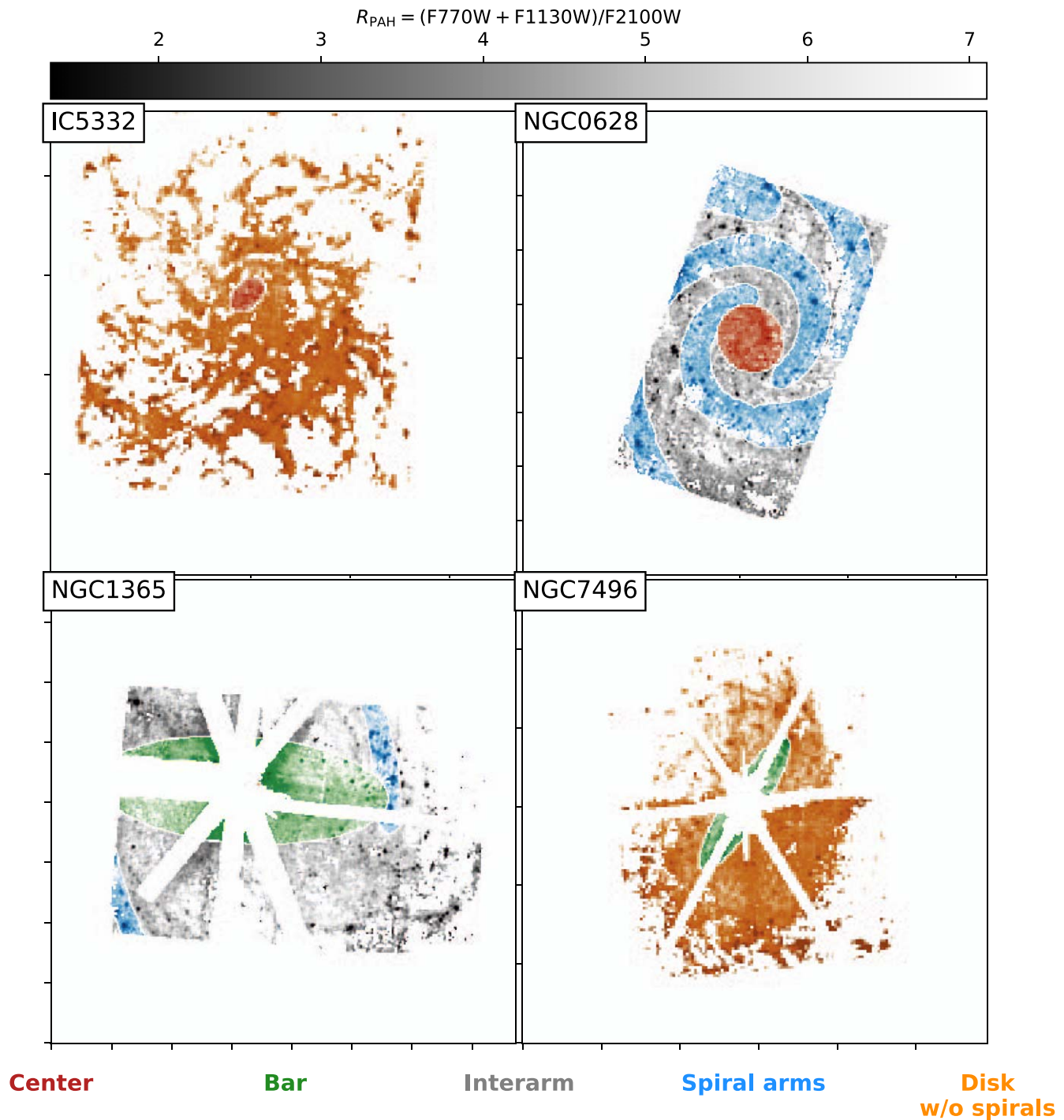


**Figure 4.**  $R_{\text{PAH}}$  maps colored by the environmental masks from Querejeta et al. (2021): center in red, bar in green, interarms in gray, spiral arms in blue, and disk in orange. We use this separation to measure the median  $R_{\text{PAH}}$  in each phase individually, and collectively, in Figure 2.

Voronoi binning, to check whether the trends seen in Figure 2 would be significantly pulled down by taking into account more low-S/N pixels.

#### 4. Conclusions

With the advent of the JWST, we can now probe individual mid-IR emission features on spatial scales never achieved before outside the Local Group. In this Letter, we have used a combination of the JWST/MIRI F770W, F1130W, and F2100W filters to trace the abundance of PAHs relative to

small dust grains in four nearby galaxies, IC 5332, NGC 628, NGC 1365, and NGC 7496, as part of the Treasury GO program PHANGS–JWST #2107.

We present maps of  $R_{\text{PAH}} \equiv (F770W + F1130W)/F2100W$  in these first four targets. This ratio traces the relative fraction of PAHs (the F770W and F1130W bands) to small dust grains (from the F2100W band). The ratio  $R_{\text{PAH}}$  decreases in H II regions, showing that the PAH fraction drops there, which is further discussed in Egorov et al. (2023). We track the variations of the abundance ratio as a function of the ISM content as traced by CO, H $\alpha$ , HI, and metallicity measurements.



We find that  $R_{\text{PAH}}$  as a function of ionized gas fraction (traced by  $I_{\text{H}\alpha}/\Sigma_{\text{H}\text{I}+\text{H}\text{2}}$ , Figure 2, bottom left panel) shows a similar trend in all the targets: a rather flat distribution up to a value of  $I_{\text{H}\alpha}/\Sigma_{\text{H}\text{I}+\text{H}\text{2}} \sim 10^{37.5} \text{ erg s}^{-1} \text{ kpc}^{-2} (M_{\odot} \text{ pc}^{-2})^{-1}$  for all galaxies, at which the abundance ratio systematically decreases. The variations with the fraction of molecular gas (Figure 2, bottom right panel) are rather small. This work sets the stage for future research to refine how the local environment influences the relative PAH fraction. As JWST data reduction methods are improved and the sample of galaxies with this coverage expands, the conditions in which PAHs are found will be better established. This early study provides insights into how global metallicity and ISM environment can effect the relative PAH population and shows the improvements that JWST observations bring to determining the answers to these questions.

We thank the anonymous referee for careful reading and comments that helped improve the clarity of the paper. This work was carried out as part of the PHANGS collaboration, associated with JWST program 2107. This work is based on observations made with the NASA/ESA/CSA JWST. Some/all of the data presented in this paper were obtained from the Mikulski Archive for Space Telescopes (MAST) at the Space Telescope Science Institute, which is operated by the Association of Universities for Research in Astronomy, Inc., under NASA contract NAS 5-03127. The specific observations analyzed can be accessed via doi:[10.17909/9bdf-jn24](https://doi.org/10.17909/9bdf-jn24). Based on observations collected at the European Southern Observatory under ESO programmes 094.C-0623 (PI: Kreckel), 095.C-0473, 098.C-0484 (PI: Blanc), 1100.B-0651 (PHANGS-MUSE; PI: Schinnerer), as well as 094.B-0321 (MAGNUM; PI: Marconi), 099.B-0242, 0100.B-0116, 098.B-0551 (MAD; PI: Carollo) and 097.B-0640 (TIMER; PI: Gadotti). This paper makes use of the following ALMA data:

ADS/JAO.ALMA#2012.1.00650.S,  
 ADS/JAO.ALMA#2013.1.01161.S,  
 ADS/JAO.ALMA#2015.1.00925.S,  
 ADS/JAO.ALMA#2015.1.00956.S,  
 ADS/JAO.ALMA#2017.1.00392.S,  
 ADS/JAO.ALMA#2017.1.00766.S,  
 ADS/JAO.ALMA#2017.1.00886.L,  
 ADS/JAO.ALMA#2018.1.01651.S,  
 ADS/JAO.ALMA#2018.A.00062.S.

ALMA is a partnership of ESO (representing its member states), NSF (USA) and NINS (Japan), together with NRC (Canada), MOST and ASIAA (Taiwan), and KASI (Republic of Korea), in cooperation with the Republic of Chile. The Joint ALMA Observatory is operated by ESO, AUI/NRAO and NAOJ.

J.C. acknowledges support from ERC starting grant #851622 DustOrigin. E.J.W. acknowledges funding from the Deutsche Forschungsgemeinschaft (DFG, German Research Foundation)—Project-ID 138713538—SFB 881 (“The Milky Way System,” subproject P1). M.C. gratefully acknowledges funding from the DFG through an Emmy Noether Research Group (grant number CH2137/1-1). COOL Research DAO is a Decentralized Autonomous Organization supporting research in astrophysics aimed at uncovering our cosmic origins.<sup>28</sup> J.M. D.K. gratefully acknowledges funding from the European





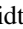



Research Council (ERC) under the European Union’s Horizon 2020 research and innovation program via the ERC Starting Grant MUSTANG (grant agreement number 714907). T.G.W. and E.S. acknowledge funding from the European Research Council (ERC) under the European Unions Horizon 2020 research and innovation program (grant agreement No. 694343). M.B. acknowledges support from FONDECYT regular grant 1211000 and by the ANID BASAL project FB210003. I.C. thanks the National Science and Technology Council for support through grants 108-2112-M-001-007-MY3 and 111-2112-M-001-038-MY3, and the Academia Sinica for Investigator Award AS-IA-109-M02. K.K., O.E. gratefully acknowledge funding from the Deutsche Forschungsgemeinschaft (DFG, German Research Foundation) in the form of an Emmy Noether Research Group (grant number KR4598/2-1, PI Kreckel). F.B. would like to acknowledge funding from the European Research Council (ERC) under the European Unions Horizon 2020 research and innovation program (grant agreement No.726384/Empire). E.R. and H.H. acknowledge the support of the Natural Sciences and Engineering Research Council of Canada (NSERC), funding reference number RGPIN-2022-03499. K.G. is supported by the Australian Research Council through the Discovery Early Career Researcher Award (DECRA) Fellowship DE220100766 funded by the Australian Government. K.G. is supported by the Australian Research Council Centre of Excellence for All Sky Astrophysics in 3 Dimensions (ASTRO 3D), through project number CE170100013. A.S. is supported by an NSF Astronomy and Astrophysics Postdoctoral Fellowship under award AST-1903834. A.K.L. gratefully acknowledges support by grants 1653300 and 2205628 from the National Science Foundation, by award JWST-GO-02107.009-A, and by a Humboldt Research Award from the Alexander von Humboldt Foundation.

*Facilities:* JWST (MIRI), MUSE, ALMA.

## ORCID iDs

Jérémy Chastenet  <https://orcid.org/0000-0002-5235-5589>  
 Jessica Sutter  <https://orcid.org/0000-0002-9183-8102>  
 Karin Sandstrom  <https://orcid.org/0000-0002-4378-8534>  
 Francesco Belfiore  <https://orcid.org/0000-0002-2545-5752>  
 Oleg V. Egorov  <https://orcid.org/0000-0002-4755-118X>  
 Kirsten L. Larson  <https://orcid.org/0000-0003-3917-6460>  
 Adam K. Leroy  <https://orcid.org/0000-0002-2545-1700>  
 Daizhong Liu  <https://orcid.org/0000-0001-9773-7479>  
 Erik Rosolowsky  <https://orcid.org/0000-0002-5204-2259>  
 David A. Thilker  <https://orcid.org/0000-0002-8528-7340>  
 Elizabeth J. Watkins  <https://orcid.org/0000-0002-7365-5791>  
 Thomas G. Williams  <https://orcid.org/0000-0002-0012-2142>  
 Ashley. T. Barnes  <https://orcid.org/0000-0003-0410-4504>  
 Frank Bigiel  <https://orcid.org/0000-0003-0166-9745>  
 Médéric Boquien  <https://orcid.org/0000-0003-0946-6176>  
 Mélanie Chevance  <https://orcid.org/0000-0002-5635-5180>  
 I-Da Chiang (江宜 達)  <https://orcid.org/0000-0003-2551-7148>  
 Daniel A. Dale  <https://orcid.org/0000-0002-5782-9093>  
 J. M. Diederik Kruijssen  <https://orcid.org/0000-0002-8804-0212>  
 Eric Emsellem  <https://orcid.org/0000-0002-6155-7166>  
 Kathryn Grasha  <https://orcid.org/0000-0002-3247-5321>

<sup>28</sup> <https://coolresearch.io/>

Brent Groves  <https://orcid.org/0000-0002-9768-0246>  
 Hamid Hassani  <https://orcid.org/0000-0002-8806-6308>  
 Annie Hughes  <https://orcid.org/0000-0002-9181-1161>  
 Kathryn Kreckel  <https://orcid.org/0000-0001-6551-3091>  
 Sharon E. Meidt  <https://orcid.org/0000-0002-6118-4048>  
 Ryan J. Rickards Vaught  <https://orcid.org/0000-0001-9719-4080>  
 Amy Sardone  <https://orcid.org/0000-0002-5783-145X>  
 Eva Schinnerer  <https://orcid.org/0000-0002-3933-7677>

## References

- Allamandola, L. J., Tielens, A. G. G. M., & Barker, J. R. 1985, *ApJL*, **290**, L25  
 Alonso-Herrero, A., Ramos Almeida, C., Esquej, P., et al. 2014, *MNRAS*, **443**, 2766  
 Anand, G. S., Lee, J. C., Van Dyk, S. D., et al. 2021, *MNRAS*, **501**, 3621  
 Aniano, G., Draine, B. T., Gordon, K. D., & Sandstrom, K. 2011, *PASP*, **123**, 1218  
 Aniano, G., Draine, B. T., Hunt, L. K., et al. 2020, *ApJ*, **889**, 150  
 Bakes, E. L. O., & Tielens, A. G. G. M. 1994, *ApJ*, **427**, 822  
 Berné, O., Fuente, A., Goicoechea, J. R., et al. 2009, *ApJL*, **706**, L160  
 Bigiel, F., & Blitz, L. 2012, *ApJ*, **756**, 183  
 Bocchio, M., Micelotta, E. R., Gautier, A. L., & Jones, A. P. 2012, *A&A*, **545**, A124  
 Bolatto, A. D., Wolfire, M., & Leroy, A. K. 2013, *ARA&A*, **51**, 207  
 Chastenet, J., Sandstrom, K., Chiang, I.-D., et al. 2019, *ApJ*, **876**, 62  
 Chastenet, J., Sutter, J., Sandstrom, K. M., et al. 2023, *ApJL*, **944**, L12  
 Chevance, M., Kruijssen, J. M. D., Hygate, A. P. S., et al. 2020, *MNRAS*, **493**, 2872  
 Chevance, M., Kruijssen, J. M. D., Krumholz, M. R., et al. 2022, *MNRAS*, **509**, 272  
 Compiègne, M., Abergel, A., Verstraete, L., & Habart, E. 2008, *A&A*, **491**, 797  
 Cortzen, I., Garrett, J., Magdis, G., et al. 2019, *MNRAS*, **482**, 1618  
 Croxall, K. V., Smith, J. D., Wolfire, M. G., et al. 2012, *ApJ*, **747**, 81  
 Dale, D. A., Cohen, S. A., Johnson, L. C., et al. 2009, *ApJ*, **703**, 517  
 den Brok, J. S., Chatzigiannakis, D., Bigiel, F., et al. 2021, *MNRAS*, **504**, 3221  
 Desert, F. X., Boulanger, F., & Puget, J. L. 1990, *A&A*, **237**, 215  
 Dong, R., & Draine, B. T. 2011, *ApJ*, **727**, 35  
 Draine, B. T. 2003, *ARA&A*, **41**, 241  
 Draine, B. T., & Li, A. 2007, *ApJ*, **657**, 810  
 Draine, B. T., Li, A., Hensley, B. S., et al. 2021, *ApJ*, **917**, 3  
 Draine, B. T., Dale, D. A., Bendo, G., et al. 2007, *ApJ*, **663**, 866  
 Egorov, O., Kreckel, L., Sandstrom, K. M., et al. 2023, *ApJL*, **944**, L16  
 Emsellem, E., Schinnerer, E., Santoro, F., et al. 2022, *A&A*, **659**, A191  
 Engelbracht, C. W., Rieke, G. H., Gordon, K. D., et al. 2008, *ApJ*, **678**, 804  
 Galliano, F. 2018, *MNRAS*, **476**, 1445  
 Galliano, F., Madden, S. C., Tielens, A. G. G. M., Peeters, E., & Jones, A. P. 2008, *ApJ*, **679**, 310  
 Galliano, F., Nersesian, A., Bianchi, S., et al. 2021, *A&A*, **649**, A18  
 García-Berete, I., Rigopoulou, D., Alonso-Herrero, A., et al. 2022, *MNRAS*, **509**, 4256  
 Giard, M., Bernard, J. P., Lacombe, F., Normand, P., & Rouan, D. 1994, *A&A*, **291**, 239  
 Gordon, K. D., Engelbracht, C. W., Rieke, G. H., et al. 2008, *ApJ*, **682**, 336  
 Groves, B., Dopita, M. A., Sutherland, R. S., et al. 2008, *ApJS*, **176**, 438  
 Groves, B., Kreckel, K., Santoro, F., et al. 2023, *MNRAS*, *Advance Access*  
 Jensen, J. J., Hönic, S. F., Rakshit, S., et al. 2017, *MNRAS*, **470**, 3071  
 Jones, A. P., Köhler, M., Ysard, N., Bocchio, M., & Verstraete, L. 2017, *A&A*, **602**, A46  
 Kennicutt, R. C., & Evans, N. J. 2012, *ARA&A*, **50**, 531  
 Kim, J., Chevance, M., Kruijssen, J. M. D., et al. 2022, *MNRAS*, **516**, 3006  
 Kreckel, K., Ho, I. T., Blanc, G. A., et al. 2019, *ApJ*, **887**, 80  
 Kruijssen, J. M. D., Schrub, A., Chevance, M., et al. 2019, *Natur*, **569**, 519  
 Lai, T. S. Y., Smith, J. D. T., Baba, S., Spoon, H. W. W., & Imanishi, M. 2020, *ApJ*, **905**, 55  
 Lai, T. S. Y., Armus, L. U. V., U, V., et al. 2022, *ApJ*, **941**, L36  
 Leboutteiller, V., Brandl, B., Bernard-Salas, J., Devost, D., & Houck, J. R. 2007, *ApJ*, **665**, 390  
 Lee, A., Sandstrom, K. M., Leroy, A. K., et al. 2023, *ApJL*, **944**, L17  
 Leroy, A. K., Bigiel, F., de Blok, W. J. G., et al. 2012, *AJ*, **144**, 3  
 Leroy, A. K., Lee, C., Schrub, A., et al. 2013, *ApJL*, **769**, L12  
 Leroy, A. K., Hughes, A., Liu, D., et al. 2021a, *ApJS*, **255**, 19  
 Leroy, A. K., Rosolowsky, E., Usero, A., et al. 2022, *ApJ*, **927**, 149  
 Leroy, A. K., Sandstrom, K., Rosolowsky, E., et al. 2023, *ApJL*, **944**, L9  
 Leroy, A. K., Schinnerer, E., Hughes, A., et al. 2021b, *ApJS*, **257**, 43  
 Li, A. 2020, *NatAs*, **4**, 339  
 Madden, S. C., Galliano, F., Jones, A. P., & Sauvage, M. 2006, *A&A*, **446**, 877  
 Makarov, D., Prugniel, P., Terekhova, N., Courtois, H., & Vauglin, I. 2014, *A&A*, **570**, A13  
 Maragkoudakis, A., Boersma, C., Temi, P., Bregman, J. D., & Allamandola, L. J. 2022, *ApJ*, **931**, 38  
 Maragkoudakis, A., Peeters, E., & Ricca, A. 2020, *MNRAS*, **494**, 642  
 Marble, A. R., Engelbracht, C. W., van Zee, L., et al. 2010, *ApJ*, **715**, 506  
 Mathis, J. S., Mezger, P. G., & Panagia, N. 1983, *A&A*, **128**, 212  
 Micelotta, E. R., Jones, A. P., & Tielens, A. G. G. M. 2010, *A&A*, **510**, A37  
 Nersesian, A., Xilouris, E. M., Bianchi, S., et al. 2019, *A&A*, **624**, A80  
 Peeters, E., Spoon, H. W. W., & Tielens, A. G. G. M. 2004, *ApJ*, **613**, 986  
 Perrin, M. D., Sivaramakrishnan, A., Lajoie, C.-P., et al. 2014, *Proc. SPIE*, **9143**, 91433X  
 Pety, J., Teyssier, D., Fossé, D., et al. 2005, *A&A*, **435**, 885  
 Pope, A., Wagg, J., Frayer, D., et al. 2013, *ApJ*, **772**, 92  
 Querejeta, M., Schinnerer, E., Meidt, S., et al. 2021, *A&A*, **656**, A133  
 Rapacioli, M., Joblin, C., & Boissel, P. 2005, *A&A*, **429**, 193  
 Regan, M. W., Thornley, M. D., Vogel, S. N., et al. 2006, *ApJ*, **652**, 1112  
 Rémy-Ruyer, A., Madden, S. C., Galliano, F., et al. 2015, *A&A*, **582**, A121  
 Rieke, G. H., Wright, G. S., Böker, T., et al. 2015, *PASP*, **127**, 584  
 Rigopoulou, D., Barale, M., Clary, D. C., et al. 2021, *MNRAS*, **504**, 5287  
 Salgado, F., Berné, O., Adams, J. D., et al. 2016, *ApJ*, **830**, 118  
 Sandstrom, K. M., Bolatto, A. D., Bot, C., et al. 2012, *ApJ*, **744**, 20  
 Santoro, F., Kreckel, K., Belfiore, F., et al. 2022, *A&A*, **658**, A188  
 Schinnerer, E., Hughes, A., Leroy, A., et al. 2019, *ApJ*, **887**, 49  
 Schrub, A., Leroy, A. K., Walter, F., et al. 2011, *AJ*, **142**, 37  
 Shipley, H. V., Papovich, C., Rieke, G. H., Brown, M. J. I., & Moustakas, J. 2016, *ApJ*, **818**, 60  
 Siebenmorgen, R., Krügel, E., & Spoon, H. W. W. 2004, *A&A*, **414**, 123  
 Smith, J. D. T., Draine, B. T., Dale, D. A., et al. 2007, *ApJ*, **656**, 770  
 Thilker, D. A., Boissier, S., Bianchi, L., et al. 2007, *ApJS*, **173**, 572  
 Tielens, A. G. G. M. 2008, *ARA&A*, **46**, 289  
 Verstraete, L. 2011, in *EAS Publications Series*, ed. C. Joblin & A. G. G. M. Tielens, Vol. 46 (Les Ulis: EDP Sciences), **415**  
 Viaene, S., Nersesian, A., Fritz, J., et al. 2020, *A&A*, **638**, A150  
 Walter, F., Brinks, E., de Blok, W. J. G., et al. 2008, *AJ*, **136**, 2563  
 Weingartner, J. C., & Draine, B. T. 2001, *ApJS*, **134**, 263  
 Williams, T. G., Kreckel, K., Belfiore, F., et al. 2022, *MNRAS*, **509**, 1303  
 Wolfire, M. G., Vallini, L., & Chevance, M. 2022, *ARA&A*, **60**, 247  
 Wong, T., Xue, R., Bolatto, A. D., et al. 2013, *ApJL*, **777**, L4  
 Zhen, J., Rodriguez Castillo, S., Joblin, C., et al. 2016, *ApJ*, **822**, 113  
 Zubko, V., Dwek, E., & Arendt, R. G. 2004, *ApJS*, **152**, 211